

Isolation control for inertially stabilized platform based on nonlinear friction compensation

Shuang Cong · Ke Deng · Weiwei Shang ·
Dejie Kong · Honghai Shen

Received: 20 November 2014 / Accepted: 11 December 2015 / Published online: 23 December 2015
© Springer Science+Business Media Dordrecht 2015

Abstract The nonlinear friction modeling and feed-forward compensation of the velocity-stabilized loop in inertially stabilized platform and closed-loop control system are studied in this paper. In order to obtain higher precision performance, an improved Stribeck friction model is proposed and designed according to the actual experimental data, whose parameters are identified by the genetic algorithm. The feed-forward compensation strategy is based on the improved model. The chattering problem and limit cycle, which arise from the changes of motion directions and the over compensation of the friction, are avoided by optimizing the compensation strategy. The actual experimental results demonstrate that the isolation performances of tracking system and carrier turbulence isolation system are superiority to the corresponding control systems without the compensations of nonlinear friction model proposed. This work has a great significance in actual applications.

Keywords Inertially stabilized platform · Non-linear friction · Parameter identification · Friction compensation

S. Cong (✉) · K. Deng · W. Shang
Department of Automation, University of Science and
Technology of China, Hefei, China
e-mail: scong@ustc.edu.cn

D. Kong · H. Shen
Changchun Institute of Optics, Fine Mechanics and Physics, Chi-
nese Academy of Science, Changchun, China

1 Introduction

Inertially stabilized platforms (ISPs) are the core devices of inertial technology application systems such as navigation, guidance and measurement. They are widely utilized in the civilian and military projects, especially in the electronic telescopes, vehicles and ships, satellites, aircraft and spacecraft [1–3]. ISPs are usually used to isolate the carrier turbulence, so that they can hold the optical axis steady to make the optic-electronic measure equipment keep the orientation to inertial space and track the target according to the command [4]. Along with the technological development and requirements increase in actual systems, there is a clear demand for high-performance ISPs. In general, the main performance indexes of ISPs include the stabilization accuracy of optical axis, optical system performance and platform loading capacity. Because of affecting the image quality directly, the stabilization accuracy of optical axis intuitively reflects the capability of isolating the carrier turbulence, which has reached micro-radian magnitude order. At present, there are mainly two ways for improving the stabilization accuracy of optical axis: one way is to design advanced control algorithm to enhance the isolation of the velocity-stabilized loop; the other way is to make use of new driving and stabilization structure, for instance, to introduce fast optical stabilization technology in existing mechanical structure [5]. Under the given structure and hardware of a platform, the key point to improve further the stabilization accuracy is to analyze clearly reasons

caused the residual errors in velocity control system and then adopt proper control strategy to further eliminate or compensate for those residual errors to achieve a higher control accuracy. Typically, the accurate modeling compensation for the platform with nonlinear friction effect is an important and directly effective control approach.

ISPs are complicated high-precision control systems integrated by the optics, mechanics and electrics. Moreover, they are suffered by various disturbances such as disturbing torque, gyro drift and mechanical resonance, in which the nonlinear friction is mainly representative. In the requirements of turbulence isolation performance with low-velocity, and low-frequency conditions of ISPs, nonlinear friction is the leading factor of performance degeneration [6,7] which may lead to steady-state error or oscillation [8]. Nowadays, the friction compensation becomes a necessary step for designing a high-precision control system. Therefore, the nonlinear friction compensation and its engineering implementation [9] have been the research hotspots. The model-based friction compensation is one of the important strategies, and the key issues are the establishment of proper friction model and the estimation of significant parameters of the model [10]. Up to now, there have been existed many friction models [11], which can be divided into two types: static friction and dynamic friction models [12]. The static friction models include classic friction model, Stribeck model [13], Karnopp model [14] and so on. The dynamic friction models, which can describe some phenomena that cannot be described by static friction models such as friction hysteresis and friction lag, are divided into physical model [15], empirical model represented by Dahl model [16] and LuGre model [17], and mixed model represented by GMS model [18]. The static friction model owns simple structure and high engineering practicability, but it has low accuracy and switch-over problem. While the dynamic friction model has high accuracy, but the model structure and parameter settings are complicated. Furthermore, many adaptive friction compensation strategies [19,20] have been intensively studied to enhance the real-time compensation effects. The nonlinear observer to estimate the friction is introduced, which enables the system to generate the control quantity with the same size and an opposite direction of the estimated friction to eliminate it. On the other hand, the model-free friction compensation has a promising prospect because of the complex of real

friction. People can make use of the observer and/or advanced control strategy to suppress the aggregate disturbance of friction together with other nonlinearity [6,21]. At present, a class of methods based on a disturbance observer [22,23] is representative model-free compensation strategies.

The controlled system we interested in here is an airborne two axes four-gimbal ISP which needs the stabilization accuracy in micro-radian magnitude. In the actual flight, the ISP is affected by the turbulence, and in the control system simulation, the turbulence is simplified as an external cosine disturbance signal. The main task of the ISP now is to achieve the performance of isolating this external cosine disturbance signal with 3° amplitude and 1/6Hz frequency. The present actual ISP velocity closed-loop control system uses the PID controllers [24]. Owing to the very small amplitude and slower frequency, the dead zone in nonlinear friction becomes a great negative impact and needs to be eliminated first. In this work, we try to design an effective friction compensation strategy with high engineering practicability on the basis of the original control system to further improve the control accuracy of the actual system. We adopt model-based feed-forward compensation, and a proposed improved Stribeck friction model which was validated that it can approximately fit the actual friction with 90% accuracy [25]. The contribution of this paper is to establish the controlled system model of nonlinear friction with 24 parameters through the combination of mechanics and experiments and then obtain the more accuracy improved model by means of the actual experimental data correction. The 24 parameters with positive and negative motion directions in the system model are identified by genetic algorithm [26]. The compensation quantity is optimized to avoid the chattering problem [27] arising from the model equation switch-over and limit cycle oscillation [28] due to friction over-compensation. We give the whole control system design procedure in detail. Finally, actual experiments both in turbulence tracking system and isolation system are implemented and the experimental results are analyzed.

The rest parts of the paper are arranged as follows: Sect. 2 is the establishment of the improved Stribeck friction model. Section 3 is parameter identification based on the genetic algorithm, and the model verification. Section 4 is the actual experiments of friction feed-forward compensation, control system design and

experimental results analysis. Section 5 is the conclusion.

2 Improved Stribeck friction model establishment

The actual system with two axes four-gimbal ISP is composed by the inner azimuth gimbal, the inner elevation gimbal, the outer elevation gimbal and the outer azimuth gimbal. The outer gimbals follow the inner gimbals. With rate gyros as feedback sensors in the two inner gimbals, the velocity-stabilized loop is the key part in the isolation of carrier turbulence, whose performance influences the final stabilization accuracy of the platform directly. Here we takes the velocity-stabilized loop of the inner azimuth gimbal as an example to do the study.

2.1 Setup of integrated nonlinear model

As a usual, a second-order velocity model can be deduced a first-order inertia model for a DC torque motor, its discrete linear model can be written as:

$$\omega_2(z) = K_e \cdot \frac{bz^{-1}}{1 - az^{-1}} \cdot u(z) \tag{1}$$

where $\omega_2(z)$ is the angular velocity, $u(z)$ is the input signal, and K_e is the equivalent model for the amplifier of motor. $a = \exp(-\eta \cdot T/J)$, $b = 1/J$, and T is the sampling period of discretization, J is the moment of inertia converted to the motor shaft, and η is the viscous friction torque coefficient.

The open-loop nonlinear system model of velocity is shown in Fig. 1, in which the ‘‘Improved Stribeck Nonlinear Friction Model’’ is the nonlinear friction model to be designed, which is one of the main task in the paper, and the accuracy of this model will affect directly the effectiveness of feed-forward compensation.

The general expression of Stribeck friction model is given by [11]:

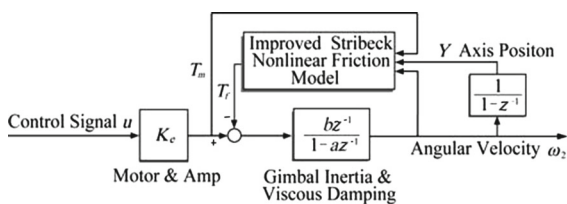


Fig. 1 Open-loop nonlinear system model of velocity

$$T_f(\omega_2, T_m) = \begin{cases} T_m & \text{if } (\omega_2 = 0) \& (|T_m| < T_s) \\ \text{sgn}(T_m) \cdot T_s & \text{if } (\omega_2 = 0) \& (|T_m| > T_s) \\ T_{\text{Stribeck}}(\omega_2) & \text{otherwise} \end{cases} \tag{2}$$

where ω_2 is the angular velocity of the rotating platform, T_m denotes driving torque of the motor, $T_f(\omega_2, T_m)$ denotes nonlinear friction torque, and T_s denotes static friction torque. $T_{\text{Stribeck}}(\omega_2)$ is the Stribeck curve which has several expressions for different application cases. According to the suggestion by Tustin [29], we select $T_{\text{Stribeck}}(\omega_2)$ as:

$$T_{\text{Stribeck}}(\omega_2) = \text{sgn}(\omega_2) \cdot [T_c + (T_s - T_c) \cdot \exp(-\alpha \cdot |\omega_2|)] \tag{3}$$

where T_c denotes Coulomb friction torque. $\alpha = |1/\omega_{\text{Stribeck}}|$ and $\alpha \in (0, 1)$. ω_{Stribeck} is the Stribeck velocity.

The classical Stribeck friction model Eqs. (2), and (3) describes the friction torque with exponential function when the velocity is other than zero. The value of friction torque is between T_c and T_s , and the transition process depends upon α . It should be noted that this model only considers the friction is relevant to the angular velocity. However, we find that in our ISP system the actual friction is not only relevant to the movement directions but also to the position of the platform, due to factors such as uneven counterweights, surface materials and conductor constraint. Figure 2 shows the actual open-loop system response of the inner azimuth gimbal with the input signal:

$$u_{0.5\text{Hz}}(t) = 950 \cdot \cos(2 \cdot \pi \cdot 0.5 \cdot t) \tag{4}$$

where $u_{0.5\text{Hz}}(t)$ is the input voltage in digit value. Because the controlled system is a high-precision position tracking system, the signal of $f = 0.5\text{Hz}$ is the lowest frequency repetitive signal we can obtain from the actual open velocity system. The sampling period is $T = 1$ ms. The output angular velocity ω_2 is measured by flexible gyro in deg/sec, and the output angular position Y is measured by the resolver in deg. The peak values of ω_2 and its dead zones are estimated by the programming calculation.

From Fig. 2a one can see that there are dead zones in which each starting point is the moment that the velocity equals to zero at the first time, and the ending point is the moment that the velocity equals to zero at the last time. The peak values of ω_2 during the positive and negative movements are 11.9783 and -9.7475 °/s,

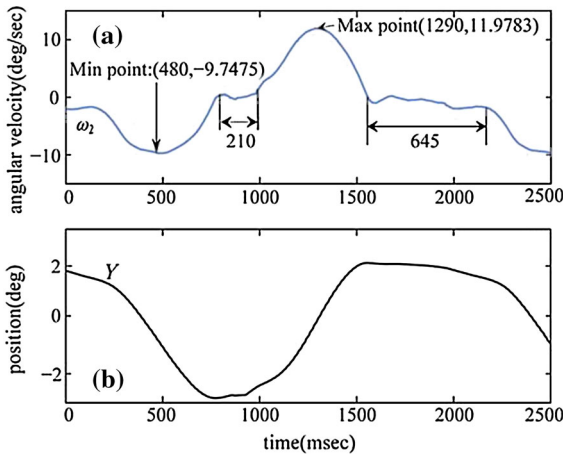


Fig. 2 Actual open-loop system response of the inner azimuth gimbal in which **a** angular velocity of the gimbal, **b** angular position of the gimbal

respectively, which means the frictions during positive and negative movement directions are asymmetry. On the other hand, comparing Fig. 2a with b, one can see the length of the dead zone in $Y > 0$ position is about 645 ms, and about 210 ms in $Y \leq 0$ position, which

indicate the friction is obviously relevant to the angular position Y . The movement of the inner azimuth gimbal is shown Fig. 3, in which the X axis is the optical axis of optic-electronic equipment when the gimbal is at the center 0° position. The Y axis is the range of the rotation angle, and it is between $\pm 4^\circ$. Thus $Y \leq 0$ indicates that the position is on the left half plane, and $Y > 0$ indicates that the position is on the right half plane. Suppose the velocity ω_2 is the positive direction of movement when the gimbal moves from the left half plane to the right half plane, and the movement direction changes the negative direction in opposite condition. Hence, the complete movement of the inner azimuth gimbal is consisted of four sub-movements of a, b, c and d as shown in Fig. 3, in which superscripts “+” and “-” are used to mark the parameters in the positive and negative direction movements, and subscripts “L” and “R” are used to mark the left and right half planes, respectively.

According to the movement analysis of inner actual azimuth gimbal in Fig. 3, an improved Stribeck non-linear friction model with high accuracy is proposed as shown in Eq. (5), in which there are 12 parameters to be identified and the meanings of the parameters are defined in Table 1 [30].

$$T_f(\omega_2, T_m, Y) = \begin{cases} \begin{cases} \xrightarrow{\omega_2 > 0} \text{sgn}(\omega_2) \cdot [T_{cL}^+ + (T_{sL}^+ - T_{cL}^+) \cdot \exp(-\alpha_L^+ \cdot |\omega_2|)] \\ \xrightarrow{\omega_2 < 0} \text{sgn}(\omega_2) \cdot [T_{cL}^- + (T_{sL}^- - T_{cL}^-) \cdot \exp(-\alpha_L^- \cdot |\omega_2|)] \\ \xrightarrow{\omega_2 = 0} \begin{cases} 0 & \text{if } T_m = 0 \\ T_m & \text{if } (T_m > 0 \ \& \ T_m < T_{sL}^+) \text{ or } (T_m < 0 \ \& \ T_{sL}^- < T_m) \\ T_{sL}^+ & \text{if } T_m > 0 \ \& \ T_m > T_{sL}^+ \\ T_{sL}^- & \text{if } T_m < 0 \ \& \ T_{sL}^- > T_m \end{cases} \end{cases} \\ \xrightarrow{Y \leq 0} \\ \begin{cases} \xrightarrow{\omega_2 > 0} \text{sgn}(\omega_2) \cdot [T_{cR}^+ + (T_{sR}^+ - T_{cR}^+) \cdot \exp(-\alpha_R^+ \cdot |\omega_2|)] \\ \xrightarrow{\omega_2 < 0} \text{sgn}(\omega_2) \cdot [T_{cR}^- + (T_{sR}^- - T_{cR}^-) \cdot \exp(-\alpha_R^- \cdot |\omega_2|)] \\ \xrightarrow{\omega_2 = 0} \begin{cases} 0 & \text{if } T_m = 0 \\ T_m & \text{if } (T_m > 0 \ \& \ T_m < T_{sR}^+) \text{ or } (T_m < 0 \ \& \ T_{sR}^- < T_m) \\ T_{sR}^+ & \text{if } T_m > 0 \ \& \ T_m > T_{sR}^+ \\ T_{sR}^- & \text{if } T_m < 0 \ \& \ T_{sR}^- > T_m \end{cases} \end{cases} \\ \xrightarrow{Y > 0} \end{cases} \quad (5)$$

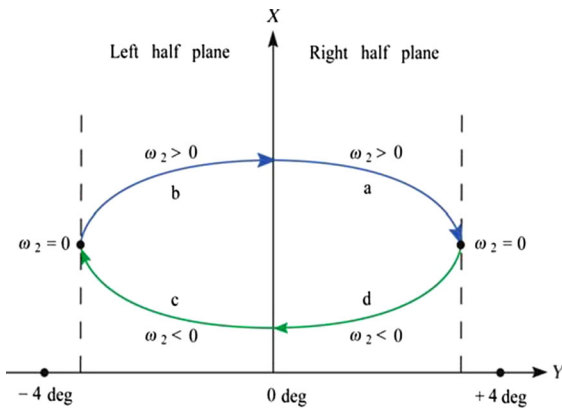


Fig. 3 Four phases of movement of the inner azimuth gimbal

Table 1 Meanings of parameters in improved Stribeck friction model

Parameters	Meanings
Y	Angular position of the inner azimuth gimbal
ω_2	Angular velocity of the inner azimuth gimbal
T_m	Driving torque of DC torque motor
$T_{sL}^+, T_{cL}^+, \alpha_L^+$	Static friction torque, Coulomb friction torque and curve factor for the “b” sub-movement
$T_{sL}^-, T_{cL}^-, \alpha_L^-$	Static friction torque, Coulomb friction torque and curve factor for the “c” sub-movement
$T_{sR}^+, T_{cR}^+, \alpha_R^+$	Static friction torque, Coulomb friction torque and curve factor for the “a” sub-movement
$T_{sR}^-, T_{cR}^-, \alpha_R^-$	Static friction torque, Coulomb friction torque and curve factor for the “d” sub-movement

Based on Eqs. (1)–(5), we can obtain the discrete relation between the system output $\omega_2(k)$ and the input $u(k - 1)$ of the system as:

$$\omega_2(k) = a \cdot \omega_2(k - 1) + b \cdot K_e \cdot u(k - 1) - b \cdot \text{sgn}(\omega_2(k - 1)) \cdot [T_c + (T_s - T_c) \cdot \exp(-\alpha \cdot |\omega_2(k - 1)|)] \quad (6)$$

in which there are 6 parameters to be identified: a , b , K_e of the linear model, and T_s , T_c , α of the nonlinear friction model. After considering the differences of movement directions and positions, the number of parameters will be 24.

The models expressed by Eqs. (5) and (6) have two characteristics: (1) nonlinearity: 4 classifications and 24 parameters; (2) the parameter b is associated with K_e , T_s and T_c . Some traditional identification methods such as Least Squares Identification may bring the difficulty owing to the multi-parameters and local optimization problems.

The improved model refines the friction according to the characteristics of the actual platform system; thus, it has higher accuracy. However, there are two problems to be solved: (1) Parameters identifications for the multi-parameter nonlinear model; (2) Chattering appeared during switch-over of the multi-model Eq. (5). These two problems will be solved separately in Sects. 3 and 4.

3 Parameters identification of nonlinear modeling

3.1 Parameter identification based on the genetic algorithm

There are three aspects of actual operation conditions should be noticed: (1) the operation condition is normally below 1 Hz; (2) the rotation angle of the inner gimbal is of narrow range between $\pm 4^\circ$; (3) the friction torques and the unbalanced torques make the biases of platform movements. Hence, the modeling input data should be of low-frequency signal, and additional input signal should be added to avoid the inner gimbal collision with the outer gimbal. Also worth noting is that the real system turbulence input signal has the frequency of 1/6 Hz. However, the lowest frequency data we could obtain in the open-loop velocity system is 0.5 Hz. Indeed the different input signals can vary the parameter values identified due to the nonlinearity of friction; however, now that our control objective is very clear and the work frequency is fix. On the one hand, we find that the lower the frequency is, the worse the performance is. On the other hand, the parameters obtained in lower frequency may not worse the performances in the case of higher frequency, but not vice versa. According to the actual system’s situation, we select the cosine input signal is:

$$u'_{0.5\text{Hz}}(t) = 950 \cdot \cos(2 \cdot \pi \cdot 0.5 \cdot t) - 200 \quad (7)$$

where $u'_{0.5\text{Hz}}(t)$ is the input control signal used in the identification, the additional value of -200 is used to

Table 2 Results of the parameters identification with 95 % confidence level for four sets of sample data

Par.	Values	Par.	Values	Par.	Values	Par.	Values
a_L^+	0.893 ± 0.00289	a_L^-	0.896 ± 0.00143	a_R^+	0.851 ± 0.00845	a_R^-	0.889 ± 0.0131
b_L^+	0.557 ± 0.00430	b_L^-	0.281 ± 0.0184	b_R^+	0.491 ± 0.0201	b_R^-	0.152 ± 0.00782
K_{eL}^+	0.0119 ± 0.000278	K_{eL}^-	0.0186 ± 0.000894	K_{eR}^+	0.00863 ± 0.000553	K_{eL}^-	0.0114 ± 0.000101
T_{cL}^+	1.950 ± 0.108	T_{cL}^-	3.569 ± 0.295	T_{cR}^+	3.176 ± 0.301	T_{cR}^-	4.016 ± 0.136
T_{sL}^+	2.743 ± 0.194	T_{sL}^-	4.254 ± 0.0565	T_{sR}^+	5.563 ± 0.284	T_{sR}^-	7.117 ± 0.139
α_L^+	0.774 ± 0.0512	α_L^-	0.166 ± 0.000501	α_R^+	0.427 ± 0.0364	α_R^-	0.263 ± 0.0137
Average MSE				0.134			

compensated for the zero drift, and the sampling period is $T = 1$ ms.

We set the parameter vector \mathbf{X} as:

$$\mathbf{X} = [a_R^+, b_R^+, K_{eR}^+, T_{sR}^+, T_{cR}^+, \alpha_R^+, a_R^-, b_R^-, K_{eR}^-, T_{sR}^-, T_{cR}^-, \alpha_R^-, a_L^+, b_L^+, K_{eL}^+, T_{sL}^+, T_{cL}^+, \alpha_L^+, a_L^-, b_L^-, K_{eL}^-, T_{sL}^-, T_{cL}^-, \alpha_L^-] \tag{8}$$

in which all parameters with sign “+” are in the positive movement direction; those parameters with sign “-” are in the negative movement direction.

We identify these 24 parameters by using the genetic algorithm. The genetic algorithm is implemented by using the calling function GA(FITNESSFCN,NVARS).m in the Global Optimization Toolbox under the MATLAB environment, which is used to find a minimum of the FITNESSFCN. The NVARS is the dimension number of design variables of FITNESSFCN. The fitness function of GA is to minimize the Mean Square Error (MSE) between the model output and the actual measured output, which can be calculated by:

$$f_{\min}(\mathbf{X}) = \min \left(\sqrt{\frac{1}{N} \cdot \sum_{i=1}^N (\omega_{\text{model}}(\mathbf{X})[i] - \omega_{\text{measured}}[i])^2} \right) \tag{9}$$

where N is the length of data sets, and $N = 2000$. $\omega_{\text{model}}(\mathbf{X})$ and ω_{measured} are the velocities of model output and measured output, respectively. All values of the selection, crossover and mutation are determined by the default values in calling function GA.m which are set in adaptive way.

In order to solve the multi-value problem that may appear in the process of identification, we limit the range of some parameters and check the rationality of some parameters with the help of the results of some auxiliary experiments.

Table 3 Results of the model verification using other four sets of data

Validate data	Data 1	Data 2	Data 3	Data 4
MSE	0.168	0.155	0.173	0.161

By means of four groups of actual sample data identification, the results of final parameters identified are shown in Table 2 in which the average MSE is 0.134% , and it is only 3.8 % of the absolute maximum amplitude of the input signal Eq. (7), which means the identification results has over 95 % confidence.

3.2 Verification of the model identified

We use other four groups of actual experimental input-output data for the verification. The results of the MSE between model outputs and measured outputs are shown in Table 3. The MSEs are <5 % of the absolute maximum amplitude of the input, which indicates the model established has sufficient accuracy. Fig. 4 is the velocity tested response of the model identified, in which Fig. 4a is the output of the model velocity ω_{model} and the actual measured output ω_{measured} , Fig. 4b is their error curves between $\omega_{\text{model}} - \omega_{\text{measured}}$.

In engineering, the performance index of the velocity-stabilized loop often used is the turbulence isolation J_ω , which is defined as:

$$J_\omega = \frac{|\omega + \omega_2|_{\max}}{|\omega|_{\max}} = \frac{|\omega_1|_{\max}}{|\omega|_{\max}} \times 100\% \tag{10}$$

where ω is the turbulence angular velocity of carrier relative to inertia space. ω_1 is the angular velocity of the platform related to inertia space. ω_2 is the angular velocity of the platform relative to the carrier. Obvi-

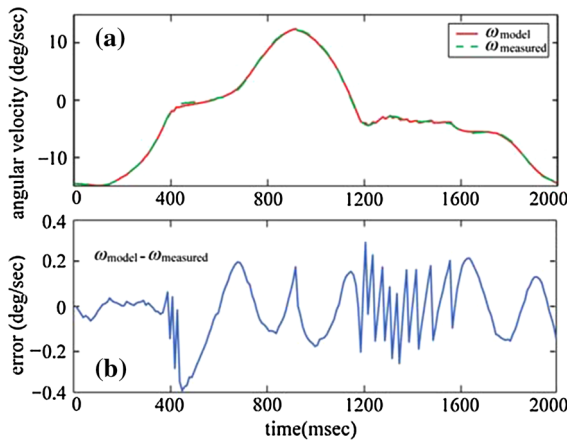


Fig. 4 Velocity tested responses of the nonlinear model identified by GA: **a** model and actual measured velocity response, **b** Error

ously, the lower of J_ω , the better performance of the isolation.

The simulation of the closed-loop control system, which is of the velocity-stabilized loop in the inner azimuth gimbal, is established. Then, the effectiveness of the model is verified by comparing simulation system with the actual system on the isolation performance. The sinusoidal signals that have three amplitudes of $\pi/2$, π and 2π with two frequencies of 1/6 and 0.5 Hz are selected as turbulence signals ω are inputted into the systems. The outputs are measured separately, and the isolations are calculated by Eq. (10). Comparison results of actual and simulation systems with different turbulences are shown in Table 4, from which one can see that the isolations of the simulation system under various turbulence inputs are very close to that of the actual system. That means the model has strong applicability.

One can also see from Table 4 that: (1) Three isolation performances in the frequency of 0.5 Hz are better than those in 1/6 Hz, which verify the increase in frequency cannot worsen the isolation; (2) For a given frequency, the smaller the amplitude is, the worse the isolation has, which means the nonlinear friction model has significant effectiveness in the case of low amplitude and low frequency; (3) The values of J_ω^{actual} are just the present isolation performances of the actual system. The isolation of control system in the signal with 1/6 Hz and π deg/sec is 22.56. Our task is to decrease further this value and increase the performance of closed-loop control system.

Table 4 Comparison isolation results of actual and simulation systems

Frequency/Hz	1/6			0.5		
Amplitude/ (deg/s)	$\pi/2$	π	2π	$\pi/2$	π	2π
$J_\omega^{actual}/(\%)$	29.89	22.56	14.28	28.24	21.37	11.78
$J_\omega^{model}/(\%)$	29.93	24.34	12.85	29.91	22.48	10.44



Fig. 5 Two axes four-gimbal ISP in actual experiments

4 Actual implementation of the friction feed-forward compensation and control system

In the actual experiments, the two axes four-gimbal ISP is fixed in 3D flight simulation turntable. The turntable provides the carrier turbulence with the angular velocity ω during flight simulation. The ISP implements the line-of-sight stabilization under the reference signal $u_{ref} = 0$, that is, keeping the angular velocity, which is of the platform relative to the inertial space, close to u_{ref} as possible. Figure 5 is the actual two axes four-gimbal ISP.

Figure 6 is the control system diagram of the carrier turbulence isolation system with feed-forward compensation of nonlinear friction. This is a feed-forward + feedback control system. Because feed-forward control does not change the characteristic equation of transfer function, this compensation does not affect the stability of feedback control system.

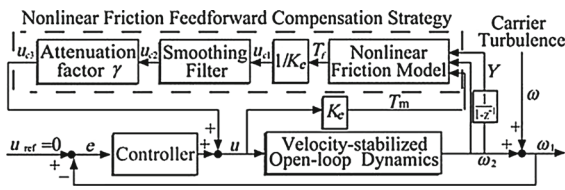


Fig. 6 Carrier turbulence isolation system with nonlinear friction feed-forward compensation

4.1 Experiments of actual turbulence tracking system

As shown in Fig. 5, in order to implement the feed-forward compensation of model friction proposed in actual system, some proper improvements should be made in the design of the model-based friction feed-forward compensation. Firstly, the compensation quantity of the friction torque T_f needs to be converted into the additional feed-forward control voltage u_{c1} , which can be described as:

$$u_{c1}(\omega_2, T_m, Y, k) = T_f(\omega_2, T_m, Y, k) / K_e \tag{11}$$

where k is the discrete time variable.

The nonlinear friction model Eq. (5) has 12 model equations. Therefore, the compensation quantity should change among these equations during actual operation, which may lead to the chattering problem [27]. To avoid the mechanical resonance or instability due to the chattering, u_{c1} needs to be smoothly filtered. With some test experiments, a smoothing three order filter u_{c2} about u_{c1} is designed as:

$$u_{c2}(k) = [u_{c1}(k) + u_{c1}(k - 1) + u_{c1}(k - 2) + u_{c1}(k - 3)] / 4 \tag{12}$$

In actual, on the one hand, under compensation of friction may lead to steady-state error, and on the other hand, over compensation may lead to limit cycle oscillation [28,31–34]. To avoid instability of the control system due to the oscillation, a conservative but effective method is used by an attenuation factor γ introduced to weaken the compensation quantity to make sure that the entire control system is in a slightly under-compensation state. So final compensation u_{c3} is:

$$u_{c3}(k) = \gamma \cdot u_{c2}(k) \tag{13}$$

where $\gamma \leq 1$. The reasonable range of γ is set as [0.90, 0.98] by means of a lot of performance test, and the optimal value is $\gamma = 0.95$.

Table 5 Isolations of PI and PI+NFC control in turbulence tracking system

Controller	Isolation J (%)					Average (%)
PI	18.54	20.84	19.01	20.46	18.68	19.47
	18.74	21.11	19.12	18.27	19.93	
PI+NFC	12.40	12.72	12.28	12.21	13.04	12.29
	11.65	11.43	12.49	11.94	12.75	

Combining Eqs. (11), (12) and (13), the final nonlinear friction compensation (NFC) $u_{c3}(k)$ can be written as:

$$u_{c3}(k) = \gamma \cdot \frac{T_f(k) + T_f(k - 1) + T_f(k - 2) + T_f(k - 3)}{4 \cdot K_e} \tag{14}$$

The input signal of the control system in this case is the angular velocity ω of carrier turbulence. Under the servo action, the angular velocity ω_2 of the platform relative to the carrier will track ω reversely, i.e. $-\omega_2 \rightarrow \omega$. In the experiments, the performance of the original control system is tested first. The closed-loop control system consists of PI controller, the notch filter and bound of control quantity. The PI controller has been debugged to optimal performance, and the proportion parameter is $K_p = 3.568$, integration parameter is $K_i = 0.0714$. Then, the performance of the original control system with friction compensation is tested. The compensation quantity is Eq. (14), and the detailed parameters of friction are provided in Table 2. The parameters of the PI controller are adjusted as $K_p = 3.0$ and $K_i = 0.15$ to make the whole control system have optimal performance. The input ω is given by $\omega_{0.5\text{Hz}}(t) = \pi \cdot \sin(2 \cdot \pi \cdot 0.5 \cdot t)$ where the amplitude is π deg/sec with the frequency $f = 0.5\text{Hz}$. The output $-\omega_2$ is in deg/sec and the sampling period is 1 ms. We separately fulfill ten experiments each for original control system (marked by PI) and the control system with the nonlinear friction compensation (marked by PI+NFC). The experimental results are shown in Table 5. Figure 7 is a comparison of velocity responses in experiments, in which the output $-\omega_{2-PI}$ of PI control and the output $-\omega_{2-PI+NFC}$ of PI+NFC control both track the turbulence ω in Fig. 7a, and their tracking errors are shown in Fig. 7b, from which one can conclude that the PI+NFC controller enhances performance over the original PI controller in four aspects:

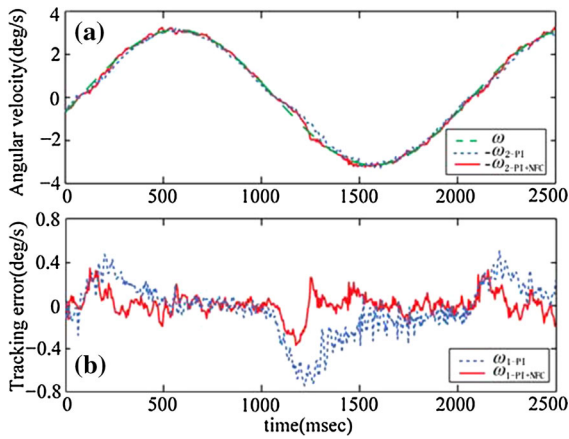


Fig. 7 Actual velocity system responses of PI and PI+NFC control in turbulence tracking system: **a** turbulence and tracking curves **b** tracking errors

- (1) Both the optimal and the worst isolation performance are improved. The optimal isolation decreases from 18.27 to 11.43%. The worst isolation decreases from 21.11 to 13.04%.
- (2) The average isolation performance is increased. The average isolation decreases from 19.47 to 12.29%. The 7.18% decreasing amplitude means the isolation performance increases 36.88% in the original basis.
- (3) The performance stability is intensified. The range of isolations decreases from 21.11–18.27% = 2.84% to 13.04–11.43% = 1.61%, and the square error decreases from 1.0616E-4 to 2.5437E-5.
- (4) The performance of tracking error is improved. The maximum absolute value of error decreases from 0.5796 to 0.3657°/s. By calculating, the mean square value of error decreases from 0.2422 to 0.1077°/s. The 0.1345°/s decreasing amplitude means the tracking error decreases 55.53% in the original basis.

4.2 Experiments of carrier turbulence isolation system

In the actual experiments, the ISP is fixed in the 3D flight simulation turntable as shown in Fig. 8. The turntable can provide sinusoidal position turbulence in azimuth, elevation and rolling, with 3° amplitude and 1/6Hz frequency as: $\omega_{1/6\text{Hz}}(t) = \pi \cdot \cos(2 \cdot \pi \cdot 1/6 \cdot t)$ where the amplitude is π deg/sec and the frequency is $f = 1/6\text{Hz}$. The azimuth control

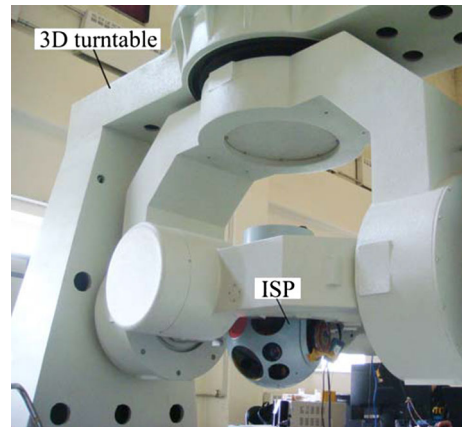


Fig. 8 3D flight simulation turntable in actual experiments

Table 6 Isolations of PI and PI+NFC control in turbulence isolation system

Controller	Isolation <i>J</i> (%)					Average (%)
PI	22.90	21.28	23.48	21.29	22.23	23.01
	22.32	24.46	25.01	24.07	23.02	
PI+NFC	12.87	14.15	13.35	13.56	13.39	13.40
	14.18	13.89	12.14	12.81	13.63	

system here requires the coordination of inner azimuth gimbal and outer azimuth gimbal. This is an important difference from the experiments in Sect. 4.1. In the integrated control system, the angular position output of the inner gimbal is the reference position input of the outer gimbal. The outer gimbal follows the inner gimbal to fulfill the expansion of rotation angle range, primary stability and turbulence isolation.

The controller parameters of the inner gimbal are as same as that in Sect. 4.1. Ten groups of experiments are conducted each for PI control and PI+NFC control, and the results are shown in Table 6. Figure 9 is actual experimental angular velocity tracking error results of turbulence isolation under the two controllers. From Table 6 and Fig. 9 one can see that comparing PI+NFC with PI, the optimal isolation decreases from 21.28 to 12.14%, the worst isolation decreases from 25.01 to 14.18%; the average isolation decreases from 23.01 to 13.40% with the decreasing amplitude of 9.61%, which means the isolation performance increases 41.76% in the original basis; the isolation range decreases from 3.73 to 2.04%, and the square error decreases from 1.6105E-4

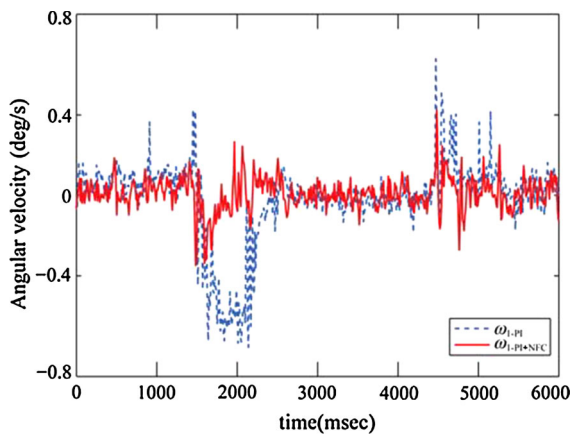


Fig. 9 Actual system experimental results of turbulence isolation under PI and PI+NFC control in carrier turbulence isolation system

to $4.1229\text{E}-5$; the maximum absolute value of ω_1 decreases from 0.7559 to 0.4192 °/s, the mean square value decreases from 0.2059 to 0.0811 °/s. In concluding, the PI+NFC controller has improved greatly the isolation performance over the original PI controller in all aspects.

5 Conclusion

The residual errors in high-precision control systems are in fact mainly caused by nonlinear friction, which also seriously impacts on isolation performances of high-precision ISP under low-velocity and low-frequency operation conditions. According to the feature of the actual platform, a more refining improved friction model was proposed based on Stribeck friction model in this paper. The nonlinear model for the velocity-stabilized loop was set up by combining the improved friction model and mechanism derived linear model, and its parameters were identified by genetic algorithm. The effectiveness of the model was verified both by testing the MSE of the data, and the isolations between simulation system and actual system. Actual experiments were separately implemented on the turbulence tracking system and the carrier turbulence isolation system. All performances including the average isolation in turbulence tracking system and in carrier turbulence isolation system were improved remarkably. The control strategy proposed in this paper demonstrated the great effectiveness in ISP and has the significantly practical value.

Acknowledgments This work was supported in part by the Projects of Ultra-Precision Control System Joint Lab. of USTC No. KD1012210167, and the National Natural Science Foundation of China under Grant No. 61573330.

References

- Hurak, Z., Rezac, M.: Image-based pointing and tracking for inertially stabilized airborne camera platform. *IEEE Trans. Control Syst. Technol.* **20**(5), 1146–1159 (2012)
- Debruin, J.: Control systems for mobile satcom antennas. *IEEE Control Syst. Mag.* **28**(1), 86–101 (2008)
- Masten, M.: Inertially stabilized platforms for optical imaging systems: tracking dynamic targets with mobile sensors. *IEEE Control Syst. Mag.* **28**(2), 47–64 (2008)
- Hilkert, J.M.: Inertially stabilized platform technology: concepts and principles. *IEEE Control Syst. Mag.* **8**(2), 26–46 (2008)
- Hilkert, J. M.: A comparison of inertial line-of-sight stabilization techniques using mirrors. In: *Proceedings of SPIE*, vol. 5430, pp. 13–22. Bellingham, WA (2004)
- Du, H.L., Satish, S.N.: Modeling and compensation of low-velocity friction with bounds. *IEEE Trans. Control Syst. Technol.* **7**(1), 10–21 (1999)
- Sun, M.W., Wang, Z.H., Wang, Y.K., Chen, Z.Q.: On low-velocity compensation of brushless DC servo in the absence of friction model. *IEEE Trans. Ind. Electron.* **60**(9), 3897–3905 (2013)
- Lee, T.H., Tan, K.K., Huang, S.N.: Adaptive friction compensation with a dynamical friction model. *IEEE/ASME Trans. Mechatron.* **16**(1), 133–140 (2011)
- Amin, J., Friedland, B., Harnoy, A.: Implementation of a friction estimation and compensation technique. *IEEE Control Syst. Mag.* **17**(4), 71–76 (1997)
- Jamaludin, Z., Brussel, H.V., Swevers, J.: Friction compensation of an XY feed table using friction-model-based feed-forward and an inverse-model-based disturbance observer. *IEEE Trans. Ind. Electron.* **56**(10), 3848–3853 (2009)
- Armstrong, B., Dupont, P., Canudas, C.: A survey of models analysis tools and compensation methods for the control of machines with friction. *Automatica* **30**(7), 1083–1138 (1994)
- Awrejcewicz, J., Olejnik, P.: Analysis of dynamic systems with various friction laws. *ASME Appl. Mech. Rev.* **58**, 389–410 (2005)
- Canudas, C.: Dynamic friction models and control design. In: *American Control Conference*, pp. 1920–26. San Francisco, CA, USA (1993)
- Karnopp, D.: Computer simulation of stick slip friction in mechanical dynamic systems. *ASME J. Dyn. Syst. Meas. Control* **107**, 100–103 (1985)
- Al-Bender, F., Lampaert, V., Swevers, J.: A novel generic model at asperity level for dry friction force dynamics. *Tribol. Lett.* **16**(1), 81–93 (2004)
- Dahl, P.R.: *Measurement of Solid Friction Parameters of Ball Bearings*. The Aerospace Corporation, EI Segundo, California (1977)
- Canudas, C., Olsson, H., Atrom, K.J.: A new model for control of systems with friction. *IEEE Trans. Autom. Control* **40**(3), 419–425 (1995)

18. Al-Bender, F., Lampaert, V., Swevers, J.: The generalized Maxwell-slip model: a novel model for friction simulation and compensation. *IEEE Trans. Autom. Control* **50**(11), 1883–1887 (2005)
19. Friedland, B., Park, Y.J.: On adaptive friction compensation. *IEEE Trans. Autom. Control* **37**(10), 1609–1612 (1992)
20. Amthor, A., Zschaeck, S., Ament, C.: High precision position control using an adaptive friction compensation approach. *IEEE Trans. Autom. Control* **55**(1), 274–278 (2010)
21. Han, J.Q.: From PID to active disturbance rejection control. *IEEE Trans. Ind. Electron.* **56**(3), 900–906 (2009)
22. Mohammadi, A., Tavakoli, M., Marquez, H.J.: Disturbance observer-based control of non-linear haptic teleoperation systems. *IET Control Theory Appl.* **5**(18), 2063–2074 (2011)
23. Huang, W., Liu, C., Hsu, P., Yeh, S.: Precision control and compensation of servomotors and machine tools via the disturbance observer. *IEEE Trans. Ind. Electron.* **57**(1), 420–429 (2010)
24. Armstrong, B., Amin, B.: PID control in the presence of static friction: a comparison of algebraic and describing function analysis. *Automatica* **32**(5), 679–692 (1996)
25. Canudas, C., Carillo, J.: A modified EW-RLS algorithm for system with bounded disturbance. *Automatica* **26**(3), 599–606 (1990)
26. Alonge, F., D’Ippolito, F., Ferrante, G., Raimondi, F.M.: Parameter identification of induction motor model using genetic algorithms. *IEE Proc. Control Theory Appl.* **145**(6), 587–593 (1998)
27. Papadopoulos, E.G., Chaspari, G.C.: Analysis and model-based control of servomechanisms with friction. *ASME J. Dyn. Syst. Meas. Control* **126**(4), 911–915 (2004)
28. Putra, D., Nijmeijer, H., Wouw, N.: Analysis of under compensation and overcompensation of friction in 1DOF mechanical systems. *Automatica* **43**(8), 1387–1394 (2007)
29. Tustin, A.: The effects of backlash and of speed dependent friction on the stability of closed-cycle control systems. *J. Inst. Electr. Eng.* **94**(2), 143–151 (1947)
30. Deng, K., Cong, S., Shang, W.W., Kong, D., Shen, H.: Non-linear friction modelling and analysis for inertially stabilized platform. In: *Hong Kong International Conference on Engineering and Applied Science (HKICEAS)*, pp. 606–611. Hong Kong (2013)
31. Saha, A., Bhattacharya, B., Wahi, P.: A comparative study on the control of friction-driven oscillations by time-delayed feedback. *Nonlinear Dyn.* **60**, 15–37 (2010)
32. Demir, O., Keskin, I., Cetin, S.: Modelling and control of a nonlinear half-vehicle suspension system: a hybrid fuzzy logic approach. *Non-linear Dyn.* **67**, 2139–2515 (2012)
33. Cheng, C., Xu, W., Shang, J.: Optimal distribution of the actuating torques for a redundantly actuated masticatory robot with two higher kinematic pairs. *Non-linear Dyn.* **79**(2), 1235–1255 (2015)
34. Hua, C., Chang, Y.: Decentralized adaptive neural network control for mechanical systems with dead-zone input. *Non-linear Dyn.* **76**(3), 1845–1855 (2014)
35. Kaan, E., Yusuf, A.: High speed CNC system design. Part: II modeling and identification of feed drives. *Int. J. Mach. Tools Manuf.* **41**(10), 1487–1509 (2001)